

THE METAL-POOR STELLAR HALO IN RAVE-TGAS AND ITS IMPLICATIONS FOR THE VELOCITY DISTRIBUTION OF DARK MATTER

JONAH HERZOG-ARBEITMAN AND MARIANGELA LISANTI
Department of Physics, Princeton University, Princeton, NJ 08544

LINA NECIB

Center for Theoretical Physics, Massachusetts Institute of Technology, Cambridge, MA 02139

ABSTRACT

The local velocity distribution of dark matter plays an integral role in interpreting the results from direct detection experiments. We previously showed that metal-poor halo stars serve as excellent tracers of the virialized dark matter velocity distribution using a high-resolution hydrodynamic simulation of a Milky Way-like halo. In this paper, we take advantage of the first *Gaia* data release, coupled with spectroscopic measurements from the RAdial Velocity Experiment (RAVE), to study the kinematics of stars belonging to the metal-poor halo within an average distance of ~ 5 kpc of the Sun. We study stars with iron abundances $[\text{Fe}/\text{H}] < -1.5$ and -1.8 that are located more than 1.5 kpc from the Galactic plane. Using a Gaussian mixture model analysis, we identify the stars that belong to the halo population, as well as some kinematic outliers. We find that both metallicity samples have similar velocity distributions for the halo component, within uncertainties. Assuming that the stellar halo velocities adequately trace the virialized dark matter, we study the implications for direct detection experiments. The Standard Halo Model, which is typically assumed for dark matter, is discrepant with the empirical distribution by $\sim 6\sigma$ and predicts fewer high-speed particles. As a result, the Standard Halo Model overpredicts the nuclear scattering rate for dark matter masses below ~ 10 GeV. The kinematic outliers that we identify may potentially be correlated with dark matter substructure, though further study is needed to establish this correspondence.

1. INTRODUCTION

Little is known about the velocity distribution of dark matter (DM) in the Solar neighborhood, and yet the details impact its detectability. For example, the rate of DM traversing the Earth and scattering off a target depends on both its velocity, as well as its interaction cross section with the material (Goodman & Witten 1985; Drukier et al. 1986). Direct detection experiments, which are built in low-background underground laboratories, aim to discover these weakly interacting particles. However, the interpretation of their results are dependent on the uncertainties associated with the local DM phase space (Freese et al. 2013; Del Nobile 2014; Green 2017). In this paper, we discuss how such uncertainties can be mitigated by empirically determining the velocity distribution of DM with astrometric measurements of the metal-poor stellar halo.

There is currently no universal form of the DM velocity distribution that is consistent with results from numerical simulations. The standard is to simply assume

that the DM velocities follow a Maxwell-Boltzmann distribution with a peak velocity of ~ 220 km/s. Referred to as the Standard Halo Model (SHM), this distribution is derived from the assumption that the DM halo is well-modeled as a collisionless gas; an isothermal distribution with mass density $\rho \sim 1/R^2$, as naively expected due to the flat rotation curve, corresponds to a Maxwellian velocity distribution (Drukier et al. 1986). Additional forms have also been suggested (Hansen & Moore 2006; Chaudhury et al. 2010; Lisanti et al. 2011; Catena & Ulio 2012; Bozorgnia et al. 2013; Fornasa & Green 2014), though they typically rely on assumptions such as equilibrium and/or isotropy of the local DM distribution.

A separate approach has been to take the velocity distribution directly from N -body simulations, which trace the multi-body gravitational interactions in a galaxy's hierarchical formation process. DM-only simulations typically find deviations from the SHM, with distributions that extend to higher velocities and show a deficit in the peak region (Vogelsberger et al. 2009; March-Russell et al. 2009; Fairbairn & Schwetz 2009; Kuhlen

et al. 2010; Mao et al. 2013). Some of this tension appears to be relieved when baryonic physics is included in the simulation (Ling et al. 2010; Pillepich et al. 2014; Bozorgnia et al. 2016; Kelso et al. 2016; Sloane et al. 2016; Bozorgnia & Bertone 2017). These results are sensitive to the different realizations of Milky Way–like halos in the simulations, which emphasizes the importance of obtaining the true velocity distribution empirically.

The challenges associated with modeling the DM’s velocity distribution have led to sustained efforts to establish astrophysics-independent analysis strategies for direct detection experiments (Fox et al. 2011b,a; Frandsen et al. 2012; Gondolo & Gelmini 2012; Herrero-Garcia et al. 2012; Del Nobile et al. 2013; Feldstein & Kahlhoefer 2014a; Fox et al. 2014; Feldstein & Kahlhoefer 2014b; Anderson et al. 2015; Blennow et al. 2015; Herrero-Garcia 2015; Gelmini et al. 2015, 2016, 2017; Gondolo & Scopel 2017; Ibarra & Rappelt 2017). These methods are primarily useful in comparing the consistency of results between different experiments. However, one still needs to know the velocity distribution to accurately infer the bounds on (or observed properties of) the DM mass and scattering cross section.

In Herzog-Arbeitman et al. (2017), we showed that metal-poor halo stars serve as effective tracers for the kinematics of the virialized DM. In the Λ CDM paradigm, this correspondence arises from the fact that the oldest stars in the halo—like the DM—originated primarily from satellites that merged with the Milky Way (White & Rees 1978; Johnston et al. 1996; Helmi et al. 1999; Helmi & White 1999; Bullock et al. 2001; Bullock & Johnston 2005; Cooper et al. 2010). Indeed, the chemodynamical properties of the stellar halo appear to be inextricably linked to the details of a galaxy’s formation history—specifically, the infall times, masses, and chemical compositions of the satellites that merged with it (Robertson et al. 2005; Font et al. 2006a,b). To probe this primordial stellar population, one can sample stars with increasingly suppressed iron abundances, $[\text{Fe}/\text{H}]$. A star’s metallicity provides hints to its origin. In particular, those that originated from low-mass satellites typically exhibit suppressed metallicity because star formation in these systems is abbreviated and turns off as it is tidally disrupted by the Milky Way.

We demonstrated the correspondence between the kinematics of the DM and metal-poor stars explicitly using the ERIS cosmological simulation (Herzog-Arbeitman et al. 2017). ERIS is one of the highest-resolution hydrodynamic simulations of a Milky Way–like galaxy (Guedes et al. 2011, 2013; Pillepich et al. 2014; Pillepich et al. 2015; Genel et al. 2014; Shen et al. 2017). The DM and stellar velocity distributions in ERIS approach each other as more metal-poor stars are considered. Further study is needed using different N -body

simulations to understand how the results drawn from ERIS generalize to different merger histories, but these initial findings suggest a promising new method to trace the local DM velocities.

To understand the implications of these findings for direct detection experiments, we must turn to observational data of the Milky Way’s inner stellar halo—see Helmi (2008) for a review. Most recently, the velocity distribution of the inner stellar halo was studied with the Sloan Digital Sky Survey (SDSS) (Ivezic et al. 2008; Juric et al. 2008; Bond et al. 2010). The sky volume analyzed encompassed distances from ~ 100 pc to 10 kpc from the Sun at $|b| > 20^\circ$. About 47,000 stars with r -band magnitude $r < 20$ were selected with iron abundance $[\text{Fe}/\text{H}] \leq -1.1$. It was found that these halo stars were well-modeled by a multivariate Gaussian distribution in spherical coordinates with dispersions $\{\sigma_r, \sigma_\theta, \sigma_\phi\} = \{141, 75, 85\}$ km/s and uncertainties ~ 5 km/s.

For the purpose of extracting the local DM velocities, we must understand whether these results remain the same as we probe more metal-poor samples located closer to the Sun. The first data release (DR1) from *Gaia* provides an exciting opportunity to achieve this (Gaia Collaboration et al. 2016; Lindgren et al. 2016). The *Tycho-Gaia* astrometric solution (TGAS) (Michalik et al. 2015) provides the full proper motions for the subset of stars with overlap in the HIPPARCOS and *Tycho-2* catalogs (ESA 1997; Høg et al. 2000; van Leeuwen 2007). Combining these results with line-of-sight velocities from the RAdial Velocity Experiment (RAVE) (Kunder et al. 2017) yields one of the most detailed maps of the six-dimensional phase space of the local stellar halo.

In this paper, we take advantage of the RAVE-TGAS (hereafter referred to as RT) catalog to study the kinematics of the metal-poor halo and to extrapolate these results to DM. Although the uncertainties on the parallaxes and proper motions of the stars have not reached their projected values for the mission’s end, the current data allows us to start developing an analysis procedure that can be refined as the observations continue to improve. As we will show, the DM velocities may be slower than typically assumed, weakening direct detection limits on nuclear scattering for DM masses below ~ 10 GeV. We also identify kinematic outliers, which could potentially be associated with DM substructure, though further study is required to confirm their origin.

This paper is organized as follows. In Sec. 2, we describe the RAVE-TGAS catalog as well as the selection cuts used to extract the halo stars. Sec. 3 describes the mixture model used to identify the halo stars and kinematic outliers, and Sec. 4 presents the results of applying the study on data. Sec. 5 explores the implications of the

recovered velocity distributions for direct detection experiments. We conclude in Sec. 6 and provide extended results in the Appendix.

2. CATALOGS AND SELECTION

2.1. *Stellar Catalogs*

Launched in 2013, *Gaia* has a nominal mission lifetime of five years and will ultimately achieve unprecedented accuracies on the positions and proper motions of stars brighter than $V = 15$ mag. DR1, which includes results from the first 14 months of the mission, contains the positions of more than a billion stars (Gaia Collaboration et al. 2016; Lindegren et al. 2016). It is possible to extract the proper motions and parallaxes for the ~ 2 million of these stars that have a match in the HIPPARCOS and *Tycho-2* catalogs. These stars, which comprise the TGAS catalog, have typical accuracies of ~ 0.3 mas on position and 1 mas/year on proper motion (Michalik et al. 2015).

Combining the TGAS catalog with the RAVE fifth data release (DR5) provides a unique opportunity to study the local phase space of the stellar halo (Kunder et al. 2017). RAVE¹ is a magnitude-limited ($9 < I < 12$) catalog of stars from the Southern hemisphere (Boeche et al. 2011; Kunder et al. 2017). DR5 includes 457,588 unique stars observed from 2003–2013. In addition to the magnitude selection, the RAVE stars within the Galactic plane ($|b| < 25^\circ$) satisfy the color requirement $J - K_s \geq 0.5$, imposed to bias the survey towards giants. All stars satisfying these magnitude and color criteria were randomly sampled. While the catalog is not volume-complete, it exhibits no kinematic or chemical biases, which is critical for the work in this paper (Wojno et al. 2016). A wealth of information is provided for the 255,922 common stars between RAVE and TGAS, including radial velocities, proper motions, chemical abundances, and stellar parameters. The combined data set provides the most detailed snapshot of the kinematics of the local stellar distribution to date.

For the iron fractions $[\text{Fe}/\text{H}]$ of the stars, we use the RAVE-on catalog (Casey et al. 2016). This catalog was built using The Cannon (Ness et al. 2015) to perform a data-driven re-analysis of the RAVE spectra. The typical uncertainty on elemental abundances in RAVE-on is ~ 0.07 dex, which is more precise than the ~ 0.2 dex errors on $[\text{Fe}/\text{H}]$ derived from the RAVE chemical pipeline (Kunder et al. 2017).

Additionally, we use the stellar distances as provided by McMillan et al. (2017). These distances are derived by combining the *Gaia* parallaxes and updated measure-

ments of T_{eff} using the Infrared Flux Method (Blackwell & Shallis 1977; Blackwell et al. 1979) with the RAVE Bayesian distance estimator (Burnett & Binney 2010; Binney et al. 2014). The combination of data sets reduces the uncertainty on the distances by nearly a factor of two from the spectrophotometric values provided in RAVE DR5.

In summary, we take the proper motions and their associated errors, as well as the galactic (l, b) and equatorial (α, δ) coordinates, from the TGAS catalog. The heliocentric radial velocities plus their associated errors are taken from the RAVE DR5 catalog. The iron fraction $[\text{Fe}/\text{H}]$ comes from the RAVE-on catalog, and the distance estimates from McMillan et al. (2017).

2.2. *Selection Cuts*

To select stars with the best radial velocities and stellar parameters, we apply the following quality cuts to the data: $\sigma(\text{HRV}) \leq 8$ km/s, $|\text{CorrectionRV}| \leq 10$ km/s, $\text{correlationCoeff} \geq 10$, $\text{SNR} \geq 20$, $\text{AlgoConv} \neq 1$, and $\text{flag_N} \neq 1$. The first three selection criteria select stars with well-measured radial velocities. The signal-to-noise ratio (SNR) requirement selects stars where the stellar parameters are determined with high-confidence. `AlgoConv` is a quality flag for the RAVE stellar parameter pipeline; if it is equal to unity, then the output of the pipeline is not reliable. The requirement on `flag_N` removes stars that are labeled as peculiar based on their spectral morphology (Matijević et al. 2012). We also remove duplicate stars with the same right ascension and declination. These quality cuts are applied to all samples analyzed in this paper.

We caution the reader that the vast majority of the stars in our sample have $\log g \lesssim 2.0$ where the RAVE parallaxes have been observed to be systematically below their TGAS values.² This, in turn, could cause the distances—and thus the velocities—of the stars in our sample to be overestimated. This systematic effect has not been accounted for in the distance estimates provided by McMillan et al. (2017) and requires further study.

Figure 1 demonstrates some basic properties of the RAVE-TGAS sample after quality cuts. The left panel shows the distribution of iron abundance $[\text{Fe}/\text{H}]$ as a function of distance off the Galactic plane, z , and galactocentric distance, R . Note that the metallicities of all stars at a given point are averaged together in the figure. The stars in the sample are fairly local, extending up to ~ 5 kpc from the plane and clustered within ~ 4 –12 kpc of the Galactic Center. The average iron abundance of the stars decreases further from the plane, as one moves

¹ <https://www.rave-survey.org/project/>

² These stars are labeled with `flag_low_logg=1` in the catalog.

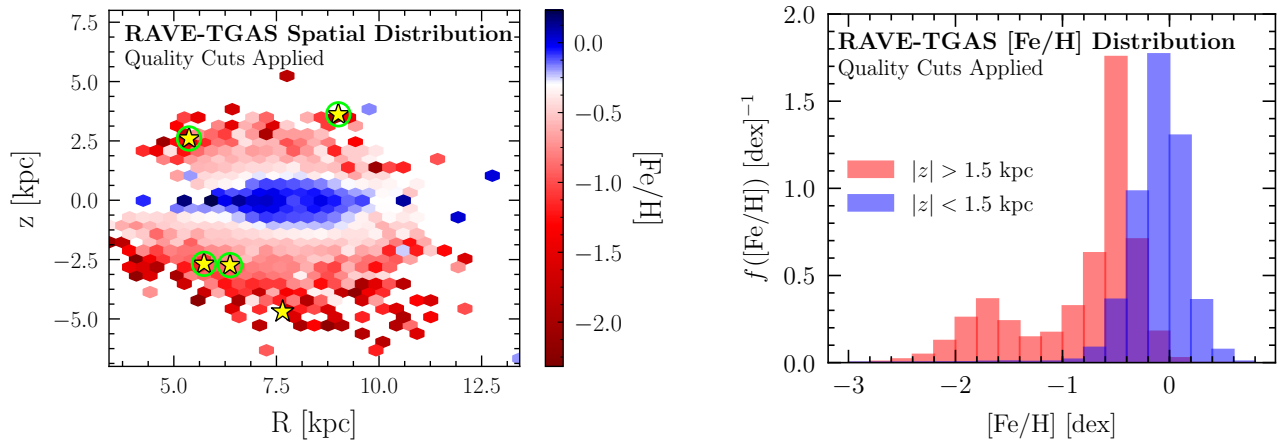


Figure 1. (Left) Distribution of the RAVE-TGAS sample in vertical distance from the Galactic plane, z , and galactocentric radius, R . The average iron abundance, $[\text{Fe}/\text{H}]$, of stars at each point is shown. The yellow stars (green circles) indicate kinematic outliers identified in the $[\text{Fe}/\text{H}] < -1.5$ (-1.8) sample. See Sec. 4 for more details. (Right) Distribution of iron abundances for the RAVE-TGAS sample, as a function of $|z|$. The low-metallicity halo component becomes more apparent farther from the plane.

from the thin/thick disk-dominated regime to the halo regime.

The right panel of Fig. 1 shows the distribution of iron abundances for stars above and below a vertical displacement of 1.5 kpc. Throughout, a distance cut $|z| > z_0$, means that there is a 95% probability that the measurement of $|z|$ passes the $|z| > z_0$ requirement. This allows us to account for the large distance errors that propagate to the magnitude of the vertical displacement. In obtaining the vertical coordinate of the stars, we assume that the Sun is located 15 pc above the Galactic mid-plane (Chen et al. 2001; Maíz-Apellániz 2001; Juric et al. 2008; Goodman et al. 2014). When $|z| < 1.5$ kpc, the distribution of iron abundance is clearly peaked at $[\text{Fe}/\text{H}] \sim 0$. As one moves further above the disk plane, the distribution shifts to lower metallicities. In particular, we see a broad peak appear at $[\text{Fe}/\text{H}] \sim -1.7$, which is consistent with the stellar halo population. This is comparable to results from SDSS, which found that the halo population is well-modeled by a Gaussian centered at $[\text{Fe}/\text{H}] = -1.46$, with a standard deviation of $\sigma_{\text{SDSS}} = 0.30$ (Ivezic et al. 2008).

In addition to the quality cuts discussed above, we also place additional selection requirements on the vertical displacement and iron abundance of the stars. To reduce contamination of disk stars, we require that the stars satisfy $|z| > 1.5$ kpc. In addition, we focus on the most metal-poor stars in the RT catalog. The two benchmark scenarios that we consider have $[\text{Fe}/\text{H}] < -1.5$ and -1.8 . The number of stars remaining after these selection cuts is 141 and 69, respectively. The stars in the $[\text{Fe}/\text{H}] < -1.5$ (-1.8) sample, range from 1.9–7 (2.7–7) kpc from the Sun, with a mean distance of 4.5 (4.7) kpc. These selection criteria are meant to iden-

tify metal-poor stars that most likely belong to the halo. We rely solely on chemical and spatial cuts to avoid potentially biasing the recovered velocity distribution through any kinematic cuts. In principle, the sample size can be improved by loosening the requirement on the vertical displacement, though one would likely need to adopt more sophisticated algorithms, such as extreme deconvolution (Bovy et al. 2011), to distinguish the halo and disk contributions—see also Beers et al. (2017).

Our cuts on the iron abundance are meant to select *ex-situ* stars, which are brought into the Milky Way through mergers. Bonaca et al. (2017) finds evidence for a metal-rich halo component in the RT catalog with $[\text{Fe}/\text{H}] \sim -1.1$. They argue that this component is likely comprised of *in-situ* stars formed within the Milky Way. As our goal here is to infer the DM velocities, we are only interested in *ex-situ* halo stars, which share a common origin with the DM in merging satellites. For this reason, we focus on stars with iron abundances below -1.5 and -1.8 . Based on our studies of the ERIS simulation (Herzog-Arbeitman et al. 2017), one would ultimately want to consider stars with even lower metallicities to feel confident in the extrapolation to DM. We discuss the convergence of our study in Sec. 5.

3. STATISTICAL METHODS

We model the velocities of the metal-poor RT sample as a mixture of two multivariate normal distributions, each defined by

$$\mathcal{N}(\mathbf{v}|\boldsymbol{\mu}, \boldsymbol{\Sigma}) = \frac{\exp\left[-\frac{1}{2}(\mathbf{v} - \boldsymbol{\mu})^T \boldsymbol{\Sigma}^{-1}(\mathbf{v} - \boldsymbol{\mu})\right]}{\sqrt{(2\pi)^3 \det(\boldsymbol{\Sigma})}}, \quad (1)$$

where $\boldsymbol{\mu}$ is the vector of means. In spherical coordinates, the covariance matrix $\boldsymbol{\Sigma}$ is defined as

$$\boldsymbol{\Sigma} = \begin{pmatrix} \sigma_r^2 & \rho_{r\theta}\sigma_r\sigma_\theta & \rho_{r\phi}\sigma_r\sigma_\phi \\ \rho_{r\theta}\sigma_r\sigma_\theta & \sigma_\theta^2 & \rho_{\theta\phi}\sigma_\theta\sigma_\phi \\ \rho_{r\phi}\sigma_r\sigma_\phi & \rho_{\theta\phi}\sigma_\theta\sigma_\phi & \sigma_\phi^2 \end{pmatrix}, \quad (2)$$

where the σ and ρ 's are the dispersions and correlation coefficients, respectively. The two distributions are intended to model the population of stars in the halo, as well as the kinematic outliers, which may be due to substructure. The procedure we adopt is a generalization of the statistical methods outlined in [Hogg et al. \(2010\)](#); [Foreman-Mackey \(2014\)](#) for outlier identification.

The data set of interest consists of N stellar velocities \mathbf{v}_i , where i labels an individual star. We use the public code `gala` ([Price-Whelan et al. 2017](#)) to perform the coordinate transformations from the ICRS frame to the spherical Galactocentric frame, with the assumption that the Sun is located at a distance of 8 kpc from the Galactic center and a vertical distance $z = 15$ pc above the plane. The errors on \mathbf{v}_i are calculated by propagating the stated uncertainties on line-of-sight velocities and proper motions, including the correlations between proper motions in right ascension and declination, assuming that they are Gaussian distributed ([Bovy 2011](#)).³ Following this prescription, we obtain measurement errors $\boldsymbol{\sigma}_i$ for each star. A given halo star is therefore drawn from a multivariate normal where each component of the dispersion is modeled as

$$\sigma_{h,i} = \sqrt{(\sigma_h)^2 + (\sigma_i)^2}, \quad (3)$$

which convolves the true dispersion of the halo distribution σ_h with the measurement error σ_i of the i^{th} star. (Note that the unbolded σ_i represents a particular component of $\boldsymbol{\sigma}_i$ in this shorthand.). The dispersions from Eq. (3) are substituted into Eq. (2), which we hereafter label as the covariance matrix $\boldsymbol{\Sigma}_{h,i}$ for star i . The same is done for the kinematic outliers, whose covariance matrix is labeled as $\boldsymbol{\Sigma}_{ko,i}$.

A flag q_i is assigned to each star, which labels whether or not it belongs to the halo—*e.g.*, $q_i = 0(1)$ for halo(outlier) stars. The likelihood for a halo star is

$$p(\mathbf{v}_i | \boldsymbol{\sigma}_i, q_i = 0, \theta) = \mathcal{N}(\mathbf{v}_i | \boldsymbol{\mu}_h, \boldsymbol{\Sigma}_{h,i}), \quad (4)$$

where the model parameters $\theta \supset (\boldsymbol{\mu}_h, \boldsymbol{\Sigma}_h)$ are the true mean and covariance of the halo distribution. Similarly, the likelihood for the kinematic outliers is

$$p(\mathbf{v}_i | \boldsymbol{\sigma}_i, q_i = 1, \theta) = \mathcal{N}(\mathbf{v}_i | \boldsymbol{\mu}_{ko}, \boldsymbol{\Sigma}_{ko,i}), \quad (5)$$

³ We ignore the uncertainties on the stellar positions in the error propagation, as they are subdominant to the uncertainties on distance and proper motion.

Parameter	Type	Priors	
		Halo	Outlier
μ_r, μ_θ	linear	$[-50, 50]$	$[-50, 50]$
μ_ϕ	linear	$[-50, 50]$	$[-400, 400]$
σ_r	log	$[10, 300]$	$[10, 1200]$
σ_θ	log	$[10, 300]$	$[100, 4000]$
σ_ϕ	log	$[5, 300]$	$[60, 4000]$
$\rho_{r\theta}, \rho_{r\phi}, \rho_{\theta\phi}$	linear	$[-1, 1]$	$[-1, 1]$
Q	log	—	$[10^{-3}, 1]$

Table 1. Parameters and associated prior types/ranges for the halo and outlier populations.

with parameters $\theta \supset (\boldsymbol{\mu}_{ko}, \boldsymbol{\Sigma}_{ko})$. It follows that the total likelihood is

$$p(\{\mathbf{v}_i\} | \{\boldsymbol{\sigma}_i\}, \{q_i\}, \theta) = \prod_{i=1}^N p(\mathbf{v}_i | \boldsymbol{\sigma}_i, q_i, \theta), \quad (6)$$

where the bracketed quantities are meant to denote the full list of N elements. The assumption that the kinematic outliers follow a normal distribution is not very important; indeed, we let the dispersions for the outliers vary over a wide range precisely to capture any stars whose velocities differ from the halo component.

At this stage, the likelihood carries a large number of free parameters, including the 18 Gaussian parameters in $\theta = (\boldsymbol{\mu}_h, \boldsymbol{\Sigma}_h, \boldsymbol{\mu}_{ko}, \boldsymbol{\Sigma}_{ko})$ and the N values of q_i . Marginalizing over the q_i reduces the likelihood to a mixture of two Gaussians:

$$p(\{\mathbf{v}_i\} | \{\boldsymbol{\sigma}_i\}, \theta) = \prod_{i=1}^N \left[(1-Q) p(\mathbf{v}_i | \boldsymbol{\sigma}_i, q_i = 0, \theta) + Q p(\mathbf{v}_i | \boldsymbol{\sigma}_i, q_i = 1, \theta) \right], \quad (7)$$

where Q is the probability that a star is an outlier. The posterior distributions for these parameters are obtained using the Markov Chain Monte Carlo `emcee` ([Foreman-Mackey et al. 2013](#)). For the results presented in this paper, we take the number of walkers to be 1200 and the number of samples per walker to be 800.

The priors are listed in Table 1. Log priors are assumed for the dispersions as well as for Q , while all other parameters have linear priors. We take much wider priors on the dispersions of the outlier population, as compared to the halo population, to reflect the assumption that the outliers have higher velocities. In addition, the prior range on μ_ϕ for the outliers is larger than the others to absorb potential contamination from disk stars.

4. KINEMATIC DISTRIBUTION

We apply the analysis strategy described in the previous section to the two separate RT samples with

Parameter	Halo Best-Fit Values	
	[Fe/H] < -1.5	[Fe/H] < -1.8
μ_r [km/s]	$0.48^{+5.80}_{-4.72}$	$0.90^{+4.32}_{-3.27}$
μ_θ [km/s]	$1.71^{+6.99}_{-3.98}$	$0.79^{+4.71}_{-3.67}$
μ_ϕ [km/s]	$1.53^{+5.21}_{-3.83}$	$0.01^{+3.55}_{-4.46}$
σ_r [km/s]	$164^{+15.7}_{-16.4}$	$178^{+27.5}_{-26.1}$
σ_θ [km/s]	$117^{+15.5}_{-16.4}$	$121^{+27.3}_{-27.9}$
σ_ϕ [km/s]	$100^{+11.8}_{-13.1}$	$96.5^{+22.6}_{-34.8}$
$\rho_{r\theta}$	$-0.18^{+0.13}_{-0.14}$	$-0.16^{+0.20}_{-0.20}$
$\rho_{r\phi}$	$-0.05^{+0.13}_{-0.13}$	$-0.15^{+0.19}_{-0.20}$
$\rho_{\theta\phi}$	$-0.04^{+0.14}_{-0.14}$	$-0.10^{+0.20}_{-0.22}$
Q	$0.09^{+0.14}_{-0.06}$	$0.14^{+0.25}_{-0.09}$

Table 2. Best-fit values (16th, 50th, and 84th percentiles) for the halo model parameters, as well as Q , the average probability that a star belongs to the outlier population.

[Fe/H] < -1.5 and -1.8. The best-fit values for the parameters (16th, 50th, and 84th percentiles of each posterior distribution) are provided in Table 2, and the full triangle plots are included in the Appendix as Figs. S1 and S2.

The top row of Fig. 2 shows the best-fit halo distributions in $v_{r,\theta,\phi}$ for the [Fe/H] < -1.5 sample.⁴ We find that the normal distribution for the halo stars is centered at $\mathbf{v} \sim 0$ km/s. The only significant velocity correlation is observed between v_r and v_θ , where $\rho_{r\theta} = -0.18^{+0.13}_{-0.14}$. This manifests as the tilt in the velocity ellipsoid in the top left panel of Fig. 2.

Repeating the analysis on the [Fe/H] < -1.8 sample, we find that the best-fit values for the parameters are generally consistent with those obtained using the higher-metallicity sample, except that the uncertainties are typically larger. Again, we find that the best-fit normal distribution for the halo is centered at zero velocity. In this case, all the correlation coefficients are consistent with zero to within their 16–84th percentiles, including $\rho_{r\theta}$ which is $-0.16^{+0.20}_{-0.20}$.

Next, we consider the population of kinematic outliers in the RT catalog. Instead of discussing the average properties of this population through its velocity distribution function, we instead take the approach of identifying and studying each outlier individually. To identify whether a star is a kinematic outlier, we calculate the probability that it belongs to the halo versus

⁴ We also show these contours in Fig. S3 overlaid with all the stars in the sample.

the outlier population. To do so, we evaluate

$$p(q_i | d, \theta) = \int p(q_i | d, \theta) p(\theta | d) d\theta \\ \approx \frac{1}{N_{\text{mc}}} \sum_{n=1}^{N_{\text{mc}}} p(q_i | d, \theta^{(n)}), \quad (8)$$

where d is shorthand for the full data set containing the velocities and errors for each star (*i.e.*, $\{\mathbf{v}_i\}, \{\sigma_i\}$). Here, $\theta^{(n)}$ denotes the set of parameters sampled in the n^{th} position of the Markov chain of length N_{mc} .

Eq. 8 allows us to recover the probability that a star in the RT sample belongs to the halo. We label star i as an outlier if

$$p(q_i = 0 | d, \theta) \leq 0.5 \quad (\text{outlier condition}). \quad (9)$$

That is, if it has a probability of less than 50% to belong to the halo. In general, we find that the stars break up cleanly into two populations above and below the 50% cutoff (see Fig. S4). The values of all chemical, spatial and kinematic properties of the outliers are listed in Table S1.

We identify five (four) stars as outliers in the [Fe/H] < -1.5 (-1.8) samples. Four of these stars are common to both; one only appears in the [Fe/H] < -1.5 analysis because its iron abundance is [Fe/H] = -1.69. The five outlier stars are giants, with surface gravities in the range $0.09 \lesssim \log g \lesssim 0.95$ dex and effective temperatures $4360 \lesssim T_{\text{eff}} \lesssim 4730$ K. These stars are metal-poor with iron abundances from $-2.56 \lesssim [\text{Fe}/\text{H}] \lesssim -1.69$. Additionally, they fall within 3.6–6.4 kpc of the Sun, and exhibit no obvious spatial clustering, as illustrated in the left panel of Fig. 1. One might note that two of these stars appear to be relatively close to each other. However, we find that their orbits are largely separated, and therefore do not believe that they are related.

The outliers are indicated as individual points in the panels of Fig. 2, where the color of each point corresponds to its probability of being a halo star, rather than an outlier. For the most part, the stars lie outside the 95% velocity contours for the halo component, with many lying outside the 99% contour. In general, the stars are distributed symmetrically around $v_{r,\phi} \sim 0$, but are skewed towards positive v_θ .

Figure 3 shows the distribution of velocities in the V_{XZ} - V_Y space, where $V_{XZ} = \sqrt{V_X^2 + V_Z^2}$ in the galactocentric cartesian frame. We show the stars for the full RT sample (*i.e.*, no $|z|$ or [Fe/H] cuts), as well as the outliers. The RT distribution is indicated by the gray-shaded region. The disk stars appear as the dark overdensity centered around $V_Y \sim 200$ km/s. The remaining halo stars are distributed at values around

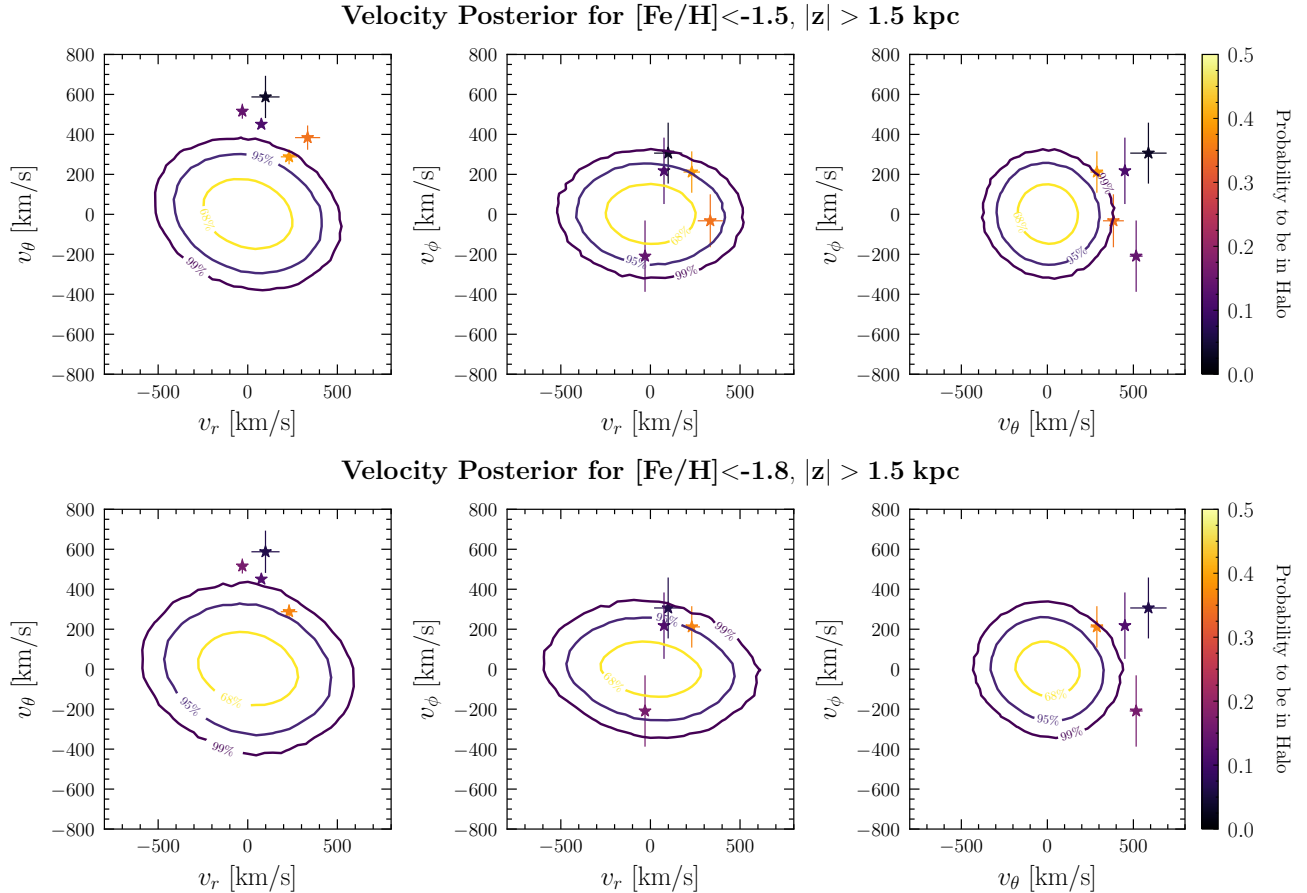


Figure 2. Posterior distributions of the spherical galactocentric velocities for the $[\text{Fe}/\text{H}] < -1.5$ analysis (top) and $[\text{Fe}/\text{H}] < -1.8$ analysis (bottom). The 68%, 95%, and 99% contours are shown in yellow, blue, and purple, respectively. The stars that are identified as kinematic outliers in each analysis are also shown. Each star’s color indicates its probability of belonging to the halo, relative to the outlier, population. The stars with the lowest probabilities tend to be located outside the 99% halo contour.

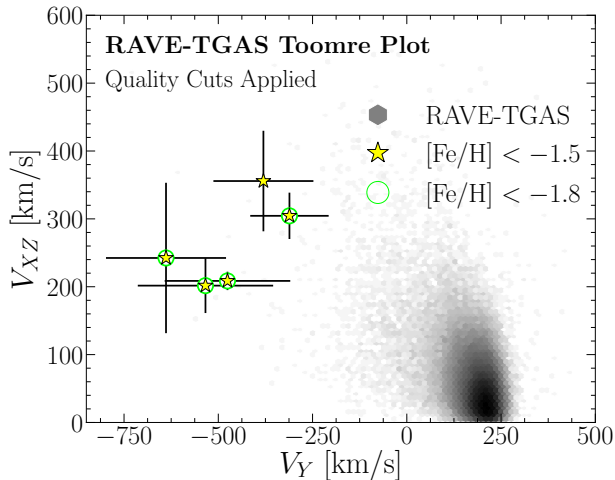


Figure 3. Toomre plot of all stars in the RAVE-TGAS catalog (shaded gray). The kinematic outliers from the $[\text{Fe}/\text{H}] < -1.5$ (-1.8) samples are indicated by the yellow stars (green circles).

$V_Y \sim 0$ km/s.⁵

The outliers for the $[\text{Fe}/\text{H}] < -1.5$ (-1.8) sample are identified as yellow stars (green circles). The error bars are computed by propagating the errors on the distances, proper motions, and heliocentric velocities (Bovy 2011). While the estimated errors are quite large, we do observe that the outliers have high velocities. Additionally, they appear to be clustered at negative V_Y and exhibit retrograde motion. We leave to future work a dedicated study of the orbits of these stars, and their potential correlation with known streams.

It is imperative to understand the origin of these stars in order to pinpoint whether we expect them to be correlated with any DM substructure. There is no overlap between our outliers and those identified in a separate study of the RAVE-TGAS data by Helmi et al. (2016).

⁵ In some instances, halo stars are selected by the kinematic cut $|V - V_{\text{LSR}}| > 220$ km/s, where $V_{\text{LSR}} = (0, 220, 0)$ km/s is the velocity of the Local Standard of Rest—see *e.g.*, Bonaca et al. (2017). We do not adopt such a cut to avoid biasing our kinematic study.

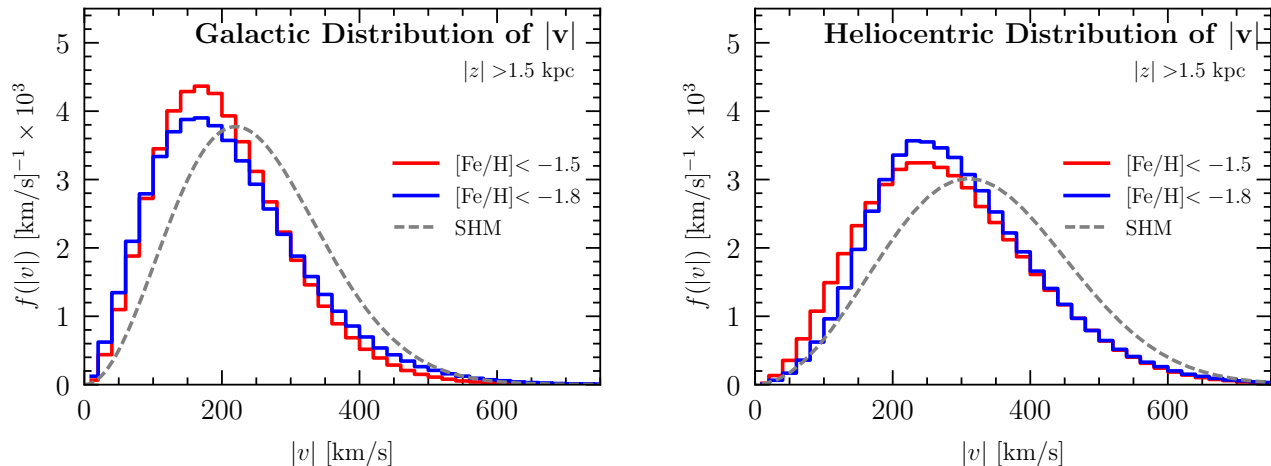


Figure 4. The posterior speed distribution for the metal-poor stars in the RAVE-TGAS halo, derived from the best-fit parameters in Tab. 2. The results for the $[\text{Fe}/\text{H}] < -1.5$ and -1.8 samples are shown separately in red and blue, respectively. The gray-dashed line represents the Standard Halo Model (SHM). The distributions are shown for the Galactic (left) and heliocentric (right) frames. Using the full nine-dimensional posterior distribution (after marginalizing over the outlier parameters), we find that the SHM is $\sim 6\sigma$ discrepant with the empirical distributions. Interpolations of the heliocentric distributions are provided as Supplementary Data.

Little information appears to be known for four of the outliers we identify, beyond their chemical and kinematic properties from RAVE and—in some cases—an entry in the Ecliptic Plane Input Catalog (Siebert et al. 2011; Munari et al. 2014; Huber et al. 2016). Improved measurements of the parallaxes and proper motions for these stars will reduce the errors on their derived velocities, while dedicated spectral studies can refine estimates of their chemical composition. Taken together, this will clarify whether these stars are *e.g.*, remnants of a globular cluster or a disrupted dwarf galaxy.

However, the star with ID ‘20070811_1523m09_120’ (also referred to as HE 1523-0901) is a very r-process enhanced metal-poor star discovered by Frebel et al. (2007). It would be interesting to trace the orbital origin of this star, in particular from other r-process dwarfs such as Reticulum II (Koposov et al. 2015; Ji et al. 2016) and Tucana III (Simon et al. 2017; Hansen et al. 2017). Metal-poor stars are likely to originate from dwarf galaxies, which can lead to DM debris when disrupted. If the origin of the kinematic outliers can be traced to dwarf galaxies, it may suggest evidence for correlated substructure in the DM phase space.

5. DARK MATTER IMPLICATIONS

In this section, we assume that the best-fit RT distributions for the metal-poor halo obtained above are adequate tracers for the kinematics of the virialized DM, and explore the implications for direct detection experiments. The left panel of Fig. 4 shows the posterior distributions for the stellar speeds in the Galactocentric frame for the $[\text{Fe}/\text{H}] < -1.5$ and -1.8 samples (red and blue lines, respectively). The two distributions are both

peaked ~ 170 km/s and are consistent with each other. The more metal-poor sample has a slightly larger dispersion, as we expect from the results presented in Sec. 4. For comparison, we also show the Standard Halo Model (SHM), defined as

$$f_{\text{SHM}}(v) = \frac{4v^2}{\sqrt{\pi}v_c^3} \exp\left[-\frac{v^2}{v_c^2}\right], \quad (10)$$

where $v_c \sim 220$ km/s is the local circular velocity (Kerr & Lynden-Bell 1986; Reid et al. 2009; McMillan & Binney 2010). We see that the RT samples have a lower average speed than expected from the SHM. Additionally, the RT distributions predict fewer high-speed particles above $v \sim 200$ km/s.

Fig. 4 shows that there is a large discrepancy between the velocity distributions of the metal-poor stars and the SHM. To quantify this difference, we marginalize over the kinematic outlier parameters in the MCMC, and integrate the resulting nine-dimensional posterior distribution for the halo parameters to find the corresponding p-value associated with the SHM. We find that the empirical distribution is $\sim 6\sigma$ discrepant with the SHM.

While our analysis method accounts for uncertainties on the measured distances and proper motions of the stars in the RT sample, it does not account for systematic biases in these measurements. As already mentioned, McMillan et al. (2017) showed that TGAS parallaxes for stars with $\log g \lesssim 2.0$ are systematically higher than those from RAVE DR5, which could over-predict the distances and, thus, the stellar velocities. About 93% (91%) of the stars in the $[\text{Fe}/\text{H}] < -1.5$ (-1.8) analysis fall in this range, and it is difficult to assess the impact on the results of our analysis. These challenges

will be ameliorated, however, as the data continues to improve with future *Gaia* data releases.

In the meantime, however, it is worthwhile understanding how the RT speed distributions could impact the scattering rates in direct detection experiments, if we assume that they effectively trace the DM distribution. To do so, we need to transform the speeds to the heliocentric frame. The results are shown in the right panel of Fig. 4.⁶ We have found that neither the Maxwell-Boltzmann distribution nor the function proposed by Mao et al. (2013) provide a satisfactory fit, and we therefore provide interpolations of the heliocentric RT distributions as tables in the Supplementary Data.⁷

The rate for a DM particle of mass m_χ to scatter off a nucleus of mass m_N is proportional to

$$g(v_{\min}) = \int_{v_{\min}}^{\infty} \frac{\tilde{f}(v)}{v} dv, \quad (11)$$

where $\tilde{f}(v)$ is the speed distribution in the lab frame and v_{\min} is the minimum DM speed needed to produce a nuclear recoil of energy E_{nr} (Jungman et al. 1996; Freese et al. 2013). Assumptions about the particle physics model for the DM candidate factor into v_{\min} . For elastic scattering,

$$v_{\min} = \sqrt{\frac{E_{\text{nr}} m_N}{2\mu^2}}, \quad (12)$$

where $\mu = m_\chi m_N / (m_\chi + m_N)$ is the reduced mass. For a specific nuclear target, v_{\min} is larger for experiments with higher energy thresholds and/or lower DM mass. In either case, $g(v_{\min})$ becomes increasingly more sensitive to the high-speed tail of the $\tilde{f}(v)$ distribution.

Figure 5 shows $\langle g(v_{\min}) \rangle$ for both the RT distributions and the SHM, where the brackets indicate the yearly average. Compared to the SHM, the scattering rate is larger by $\sim 10\%$ for the RT distributions below $v_{\min} \sim 200$ km/s, but suppressed by $\sim 40\text{--}60\%$ at larger velocities. A given direct detection experiment only probes a particular range of v_{\min} , dependent on its nuclear target and the energy range that it is sensitive to. Consider, for example, the Xenon1T experiment (Aprile et al. 2017a), which uses a xenon target to search for nuclear recoils in the range $E_{\text{nr}} = [5, 40]$ keV. For $m_\chi = 50$ GeV, this corresponds to $v_{\min} \sim 150$ km/s at threshold (*e.g.*, $E_{\text{nr}} = 5$ keV). In this case, the ratio of $\langle g(v_{\min}) \rangle$ for the RT and SHM distributions is close to unity, and the scattering rates are essentially equivalent for either velocity distribution. In contrast, when

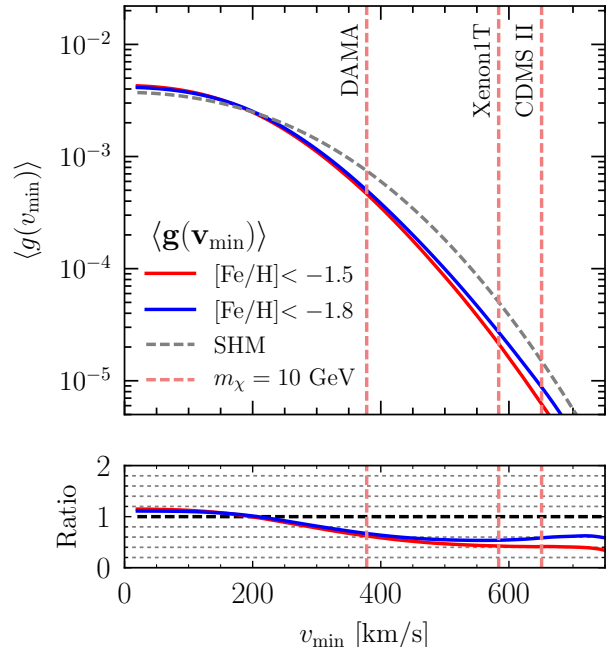


Figure 5. The function $\langle g(v_{\min}) \rangle$, defined in Eq. (11) and averaged over a year, plotted in terms of the minimum scattering velocity, v_{\min} , for the $[\text{Fe}/\text{H}] < -1.5$ and -1.8 RAVE-TGAS samples (red and blue, respectively). For comparison, we also show $\langle g(v_{\min}) \rangle$ for the SHM in dashed gray. The ratio between the RAVE-TGAS expectation and the SHM is included in the bottom panel for both iron abundances. In the top panel, we overlay the value of v_{\min} that corresponds to a 10 GeV dark matter particle scattering at threshold for the DAMA/LIBRA (Bernabei et al. 2008), Xenon1T Aprile et al. (2017b), and CDMS II (Agnese et al. 2017) experiments.

$m_\chi = 10$ GeV, then the same experiment is sensitive to $v_{\min} \sim 570$ km/s at threshold. At this minimum speed, the RT distribution results in a scattering rate that is a factor of ~ 2 smaller than that obtained with the SHM.

The dashed vertical lines in Fig. 5 indicate the value of v_{\min} that each experiment is sensitive to for a $m_\chi = 10$ GeV DM particle scattering at threshold. To compare with the Xenon1T example described above, we also show the results for the DAMA/LIBRA (Bernabei et al. 2008) and CDMS II (Agnese et al. 2015) experiments. For DAMA, a 10 GeV particle preferentially scatters off the sodium in the crystal lattice; at the threshold energy of ~ 6.7 keV, $v_{\min} \sim 350$ km/s. For CDMS II, which uses a germanium target, $v_{\min} \sim 450$ km/s for a ~ 5 keV threshold. In all these cases, the expected scattering rate is a factor of 2 too strong when the SHM is used rather than the empirical velocity distribution. These discrepancies are particularly relevant for experiments that are aimed at probing DM masses below \sim GeV. For example, CDMSlite (Agnese et al. 2017) has a low energy threshold and can probe DM masses below ~ 3 GeV, where it is sensitive to the high-speed tail of the DM distribution.

⁶ When transforming the RT posterior speed distribution to the heliocentric frame, we use the observed angular distributions of the stellar sample. The results are essentially identical if we instead assume a uniform angular distribution.

⁷ https://linoush.github.io/DM_Velocity_Distribution/

We stress that the arguments presented in this section apply to the virialized DM halo. If the kinematic outliers are associated with local DM substructure—such as streams or debris flow (Diemand et al. 2008; Vogelsberger & White 2011; Freese et al. 2004; Savage et al. 2006; Kuhlen et al. 2010; Lisanti & Spergel 2012; Kuhlen et al. 2012; Lisanti et al. 2015)—they could also impact the interpretation of the experimental results. Because the origin of these outliers is unknown, however, we choose to not include them when evaluating $\langle g(v_{\min}) \rangle$. Additionally, recent mergers of satellite galaxies could lead to spatial or kinematic substructure that is associated with more metal-rich stellar populations in the halo above $[\text{Fe}/\text{H}] \sim -1.5$. The analysis we used here cannot simply be extended to higher metallicities, where one must contend with increased contamination from disk and *in-situ* halo stars. However, it would be worthwhile to consider ways of generalizing the statistical methods of Sec. 3 to explore stellar substructure in this regime.

6. CONCLUSIONS

The primary goal of this paper was to infer the local distribution of virialized DM velocities using metal-poor stars as kinematic tracers. To achieve this, we took advantage of the RAVE-TGAS catalog, which currently provides one of the best maps of the local phase-space of the stellar halo. We conservatively required that all stars be located $|z| > 1.5$ kpc from the Galactic plane to reduce potential contamination from the disk, and considered two samples of low-metallicity stars: $[\text{Fe}/\text{H}] < -1.5$ and -1.8 . This allowed us to probe the primordial population of *ex-situ* halo stars, while still maintaining a sample size large enough for the statistical methods to converge.

To recover the velocity distribution for these stars, we used a Gaussian mixture model that accounted for both a stellar halo component and a population of kinematic outliers. The best-fit model parameters for the halo population were consistent, within uncertainties, between the $[\text{Fe}/\text{H}] < -1.5$ and -1.8 samples, despite the fact that the latter includes nearly half the number of stars as the former. The best-fit dispersions are typically larger than those found by SDSS (Bond et al. 2010) and discrepant by $\sim 4\sigma$. A precise comparison is, however, difficult to make because the SDSS observations extend over a larger sky area and include more metal-rich stars than the samples studied here.

In Herzog-Arbeitman et al. (2017), we used the Eris N -body simulation to show that metal-poor stars serve as excellent tracers for the virialized DM velocities. In the simulation, we observed that this convergence occurred for $[\text{Fe}/\text{H}] \lesssim 3$. The best we can do with the data at hand is to see how the velocity distribution changes as

progressively tighter cuts are placed on the iron abundance of the stars. Here, we found no evidence for a change in this distribution between $[\text{Fe}/\text{H}] < -1.5$ and -1.8 , though ideally one would want to continue probing even more metal-poor samples as the data continues to improve.

The posterior speed distributions of the metal-poor halo stars were obtained from the best-fit multivariate distribution. Assuming this distribution matched that of the DM, we studied the implications for direct detection experiments. Our point of comparison was the SHM, which is the most common distribution that is assumed for the DM velocities. The best-fit dispersions that we recovered are $\sim 6\sigma$ discrepant with the SHM values. For DM masses below ~ 10 GeV, the SHM typically predicts a scattering rate that is nearly a factor of two larger than what is expected from the empirical distribution.

In addition to characterizing the halo population, our analysis also identified velocity outliers. Improved kinematic and spectral studies will help determine whether these stars point to local phase-space substructure that is correlated with tidal debris from a satellite merger. If so, then the kinematic substructure in the stellar distribution may also be correlated with DM. Because we cannot make any firm conclusions at this stage, we did not consider the implications of these outliers for direct detection.

To summarize, we found the best-fit velocity distribution of the local metal-poor stellar halo using data from RAVE-TGAS and used these results to motivate an empirical distribution for the virialized dark matter component. This distribution can be used in place of the SHM for a more realistic estimate of the DM scattering rate. *Gaia* is anticipated to revolutionize our understanding of the phase-space distribution of the stellar halo. As the uncertainties on the stellar parameters continue to improve for an increasingly larger selection of stars, we expect to further refine our characterization of the smooth dark matter distribution and any potential substructure.

For the interested reader, we provide the posterior speed distributions for the $[\text{Fe}/\text{H}] < -1.5$ and -1.8 samples in the heliocentric frame as Supplementary Data.⁷

ACKNOWLEDGEMENTS

We thank S. Agarwalla, A. Bonaca, A. Frebel, D. Hogg, A. Ji, K. Johnston, A. Leder, P. Madau, A. Price-Whelan, and J. Wojno for helpful conversations. M.L. is supported by the DOE under contract DESC0007968, the Alfred P. Sloan Foundation, and the Cottrell Scholar program through the Research Corporation for Science Advancement. L.N. is supported by the DOE under contract DESC00012567.

REFERENCES

- Agnese, R., et al. 2015, *Phys. Rev.*, D92, 072003
— 2017, Submitted to: *Phys. Rev. D*, arXiv:1707.01632
- Anderson, A. J., Fox, P. J., Kahn, Y., & McCullough, M. 2015, *JCAP*, 1510, 012
- Aprile, E., et al. 2017a, arXiv:1705.06655
— 2017b, *Phys. Rev.*, D96, 022008
- Beers, T. C., Placco, V. M., Carollo, D., et al. 2017, *ApJ*, 835, 81
- Bernabei, R., et al. 2008, *Eur. Phys. J.*, C56, 333
- Binney, J., et al. 2014, *Mon. Not. Roy. Astron. Soc.*, 437, 351
- Blackwell, D. E., & Shallis, M. J. 1977, *MNRAS*, 180, 177
- Blackwell, D. E., Shallis, M. J., & Selby, M. J. 1979, *MNRAS*, 188, 847
- Blennow, M., Herrero-Garcia, J., Schwetz, T., & Vogl, S. 2015, *JCAP*, 1508, 039
- Boeche, C., Siebert, A., Williams, M., et al. 2011, *AJ*, 142, 193
- Bonaca, A., Conroy, C., Wetzell, A., Hopkins, P. F., & Keres, D. 2017, ArXiv e-prints, arXiv:1704.05463
- Bond, N. A., et al. 2010, *Astrophys. J.*, 716, 1
- Bovy, J. 2011, PhD thesis, copyright - Database copyright ProQuest LLC; ProQuest does not claim copyright in the individual underlying works; Last updated - 2016-06-04
- Bovy, J., Hogg, D. W., & Roweis, S. T. 2011, *Annals of Applied Statistics*, 5, arXiv:0905.2979
- Bozorgnia, N., & Bertone, G. 2017, arXiv:1705.05853
- Bozorgnia, N., Catena, R., & Schwetz, T. 2013, *JCAP*, 12, 050
- Bozorgnia, N., et al. 2016, *JCAP*, 1605, 024
- Bullock, J. S., & Johnston, K. V. 2005, *Astrophys. J.*, 635, 931
- Bullock, J. S., Kravtsov, A. V., & Weinberg, D. H. 2001, *Astrophys. J.*, 548, 33
- Burnett, B., & Binney, J. 2010, *Mon. Not. Roy. Astron. Soc.*, 407, 339
- Casey, A. R., Hawkins, K., Hogg, D. W., et al. 2016, ArXiv e-prints, arXiv:1609.02914
- Catena, R., & Ullio, P. 2012, *JCAP*, 5, 005
- Chaudhury, S., Bhattacharjee, P., & Cowsik, R. 2010, *JCAP*, 1009, 020
- Chen, B., Stoughton, C., Smith, J. A., et al. 2001, *ApJ*, 553, 184
- Cooper, A. P., et al. 2010, *Mon. Not. Roy. Astron. Soc.*, 406, 744
- Del Nobile, E. 2014, *Adv. High Energy Phys.*, 2014, 604914
- Del Nobile, E., Gelmini, G., Gondolo, P., & Huh, J.-H. 2013, *JCAP*, 1310, 048
- Diemand, J., Kuhlen, M., Madau, P., et al. 2008, *Nature*, 454, 735
- Drukier, A. K., Freese, K., & Spergel, D. N. 1986, *Phys. Rev.*, D33, 3495
- ESA, ed. 1997, ESA Special Publication, Vol. 1200, The HIPPARCOS and TYCHO catalogues. Astrometric and photometric star catalogues derived from the ESA HIPPARCOS Space Astrometry Mission
- Fairbairn, M., & Schwetz, T. 2009, *JCAP*, 0901, 037
- Feldstein, B., & Kahlhoefer, F. 2014a, *JCAP*, 1408, 065
— 2014b, *JCAP*, 1412, 052
- Font, A. S., Johnston, K. V., Bullock, J. S., & Robertson, B. 2006a, *Astrophys. J.*, 638, 585
- Font, A. S., Johnston, K. V., Bullock, J. S., & Robertson, B. E. 2006b, *Astrophys. J.*, 646, 886
- Foreman-Mackey, D. 2014, Blog Post: Mixture Models, Zenodo, doi:10.5281/zenodo.15856
- Foreman-Mackey, D., Hogg, D. W., Lang, D., & Goodman, J. 2013, *PASP*, 125, 306
- Fornasa, M., & Green, A. M. 2014, *Phys. Rev.*, D89, 063531
- Fox, P. J., Kahn, Y., & McCullough, M. 2014, *JCAP*, 1410, 076
- Fox, P. J., Kribs, G. D., & Tait, T. M. P. 2011a, *Phys. Rev.*, D83, 034007
- Fox, P. J., Liu, J., & Weiner, N. 2011b, *Phys. Rev.*, D83, 103514
- Frandsen, M. T., Kahlhoefer, F., McCabe, C., Sarkar, S., & Schmidt-Hoberg, K. 2012, *JCAP*, 1201, 024
- Frebel, A., Christlieb, N., Norris, J. E., et al. 2007, *ApJL*, 660, L117
- Freese, K., Gondolo, P., Newberg, H. J., & Lewis, M. 2004, *Phys. Rev. Lett.*, 92, 111301
- Freese, K., Lisanti, M., & Savage, C. 2013, *Rev. Mod. Phys.*, 85, 1561
- Gaia Collaboration, Brown, A. G. A., Vallenari, A., et al. 2016, *A&A*, 595, A2
- Gelmini, G. B., Georgescu, A., Gondolo, P., & Huh, J.-H. 2015, *JCAP*, 1511, 038
- Gelmini, G. B., Huh, J.-H., & Witte, S. J. 2016, *JCAP*, 1610, 029
— 2017, arXiv:1707.07019
- Genel, S., Vogelsberger, M., Springel, V., et al. 2014, *Mon. Not. Roy. Astron. Soc.*, 445, 175
- Gondolo, P., & Gelmini, G. B. 2012, *JCAP*, 1212, 015
- Gondolo, P., & Scopel, S. 2017, arXiv:1703.08942
- Goodman, A. A., Alves, J., Beaumont, C. N., et al. 2014, *ApJ*, 797, 53
- Goodman, M. W., & Witten, E. 1985, *Phys. Rev.*, D31, 3059
- Green, A. M. 2017, *J. Phys.*, G44, 084001
- Guedes, J., Callegari, S., Madau, P., & Mayer, L. 2011, *Astrophys. J.*, 742, 76
- Guedes, J., Mayer, L., Carollo, M., & Madau, P. 2013, *Astrophys. J.*, 772, 36
- Hansen, S. H., & Moore, B. 2006, *New Astron.*, 11, 333
- Hansen, T. T., Simon, J. D., Marshall, J. L., et al. 2017, *ApJ*, 838, 44
- Helmi, A. 2008, *A&A Rv*, 15, 145
- Helmi, A., Veljanoski, J., Breddels, M. A., Tian, H., & Sales, L. V. 2016, ArXiv e-prints, arXiv:1611.00222
- Helmi, A., & White, S. D. M. 1999, *Mon. Not. Roy. Astron. Soc.*, 307, 495
- Helmi, A., White, S. D. M., de Zeeuw, P. T., & Zhao, H.-S. 1999, *Nature*, 402, 53
- Herrero-Garcia, J. 2015, *JCAP*, 1509, 012
- Herrero-Garcia, J., Schwetz, T., & Zupan, J. 2012, *Phys. Rev. Lett.*, 109, 141301
- Herzog-Arbeitman, J., Lisanti, M., Madau, P., & Necib, L. 2017, arXiv:1704.04499
- Høg, E., Fabricius, C., Makarov, V. V., et al. 2000, *A&A*, 355, L27
- Hogg, D. W., Bovy, J., & Lang, D. 2010, ArXiv e-prints, arXiv:1008.4686
- Huber, D., Bryson, S. T., Haas, M. R., et al. 2016, *ApJS*, 224, 2
- Ibarra, A., & Rappelt, A. 2017, arXiv:1703.09168
- Ivezic, Z., et al. 2008, *Astrophys. J.*, 684, 287
- Ji, A. P., Frebel, A., Simon, J. D., & Chiti, A. 2016, *ApJ*, 830, 93
- Johnston, K. V., Hernquist, L., & Bolte, M. 1996, *Astrophys. J.*, 465, 278
- Jungman, G., Kamionkowski, M., & Griest, K. 1996, *PhR*, 267, 195
- Juric, M., et al. 2008, *Astrophys. J.*, 673, 864
- Kelso, C., et al. 2016, *JCAP*, 1608, 071
- Kerr, F. J., & Lynden-Bell, D. 1986, *Mon. Not. Roy. Astron. Soc.*, 221, 1023
- Koposov, S. E., Belokurov, V., Torrealba, G., & Evans, N. W. 2015, *ApJ*, 805, 130
- Kuhlen, M., Lisanti, M., & Spergel, D. N. 2012, *Phys. Rev.*, D86, 063505
- Kuhlen, M., Weiner, N., Diemand, J., et al. 2010, *JCAP*, 1002, 030
- Kunder, A., Kordopatis, G., Steinmetz, M., et al. 2017, *AJ*, 153, 75

- Lindegren, L., Lammers, U., Bastian, U., et al. 2016, *A&A*, 595, A4
- Ling, F. S., Nezri, E., Athanassoula, E., & Teyssier, R. 2010, *JCAP*, 1002, 012
- Lisanti, M., & Spergel, D. N. 2012, *Phys. Dark Univ.*, 1, 155
- Lisanti, M., Spergel, D. N., & Madau, P. 2015, *Astrophys. J.*, 807, 14
- Lisanti, M., Strigari, L. E., Wacker, J. G., & Wechsler, R. H. 2011, *Phys. Rev.*, D83, 023519
- Maíz-Apellániz, J. 2001, *AJ*, 121, 2737
- Mao, Y.-Y., Strigari, L. E., Wechsler, R. H., Wu, H.-Y., & Hahn, O. 2013, *Astrophys. J.*, 764, 35
- March-Russell, J., McCabe, C., & McCullough, M. 2009, *JHEP*, 05, 071
- Matijević, G., Zwitter, T., Bienaymé, O., et al. 2012, *ApJS*, 200, 14
- McMillan, P. J., & Binney, J. J. 2010, *Mon. Not. Roy. Astron. Soc.*, 402, 934
- McMillan, P. J., Kordopatis, G., Kunder, A., et al. 2017, *ArXiv e-prints*, arXiv:1707.04554
- Michalik, D., Lindegren, L., & Hobbs, D. 2015, *A&A*, 574, A115
- Munari, U., Henden, A., Frigo, A., et al. 2014, *AJ*, 148, 81
- Ness, M., Hogg, D. W., Rix, H.-W., Ho, A. Y. Q., & Zasowski, G. 2015, *ApJ*, 808, 16
- Pillepich, A., Kuhlen, M., Guedes, J., & Madau, P. 2014, *ApJ*, 784, 161
- Pillepich, A., Madau, P., & Mayer, L. 2015, *Astrophys. J.*, 799, 184
- Price-Whelan, A., Sipocz, B., Major, S., & Oh, S. 2017, *adrn/gala*, v.0.2.1, Zenodo, doi:10.5281/zenodo.833339
- Reid, M. J., et al. 2009, *Astrophys. J.*, 700, 137
- Robertson, B., Bullock, J. S., Font, A. S., Johnston, K. V., & Hernquist, L. 2005, *Astrophys. J.*, 632, 872
- Savage, C., Freese, K., & Gondolo, P. 2006, *Phys. Rev.*, D74, 043531
- Shen, S., Kulkarni, G., Madau, P., & Mayer, L. 2017, *MNRAS*, 469, 4012
- Siebert, A., Williams, M. E. K., Siviero, A., et al. 2011, *AJ*, 141, 187
- Simon, J. D., Li, T. S., Drlica-Wagner, A., et al. 2017, *ApJ*, 838, 11
- Sloane, J. D., Buckley, M. R., Brooks, A. M., & Governato, F. 2016, arXiv:1601.05402
- van Leeuwen, F. 2007, *Astron. Astrophys.*, 474, 653
- Vogelsberger, M., & White, S. D. M. 2011, *MNRAS*, 413, 1419
- Vogelsberger, M., Helmi, A., Springel, V., et al. 2009, *Mon. Not. Roy. Astron. Soc.*, 395, 797
- White, S. D. M., & Rees, M. J. 1978, *MNRAS*, 183, 341
- Wojno, J., Kordopatis, G., Piffl, T., et al. 2016, *ArXiv e-prints*, arXiv:1611.00733

APPENDIX

This Appendix includes some additional figures that supplement the discussion in the main text. Fig. S1 and Fig. S2 show the full triangle plots for the mixture model analysis performed on the RAVE-TGAS sample. Fig. S3 shows the three-dimensional velocity contours overlaid with all the stars that were analyzed. Fig. S4 histograms the stars' probabilities of belonging to the halo relative to the outlier population. Table S1 lists the kinematic outliers and their properties.

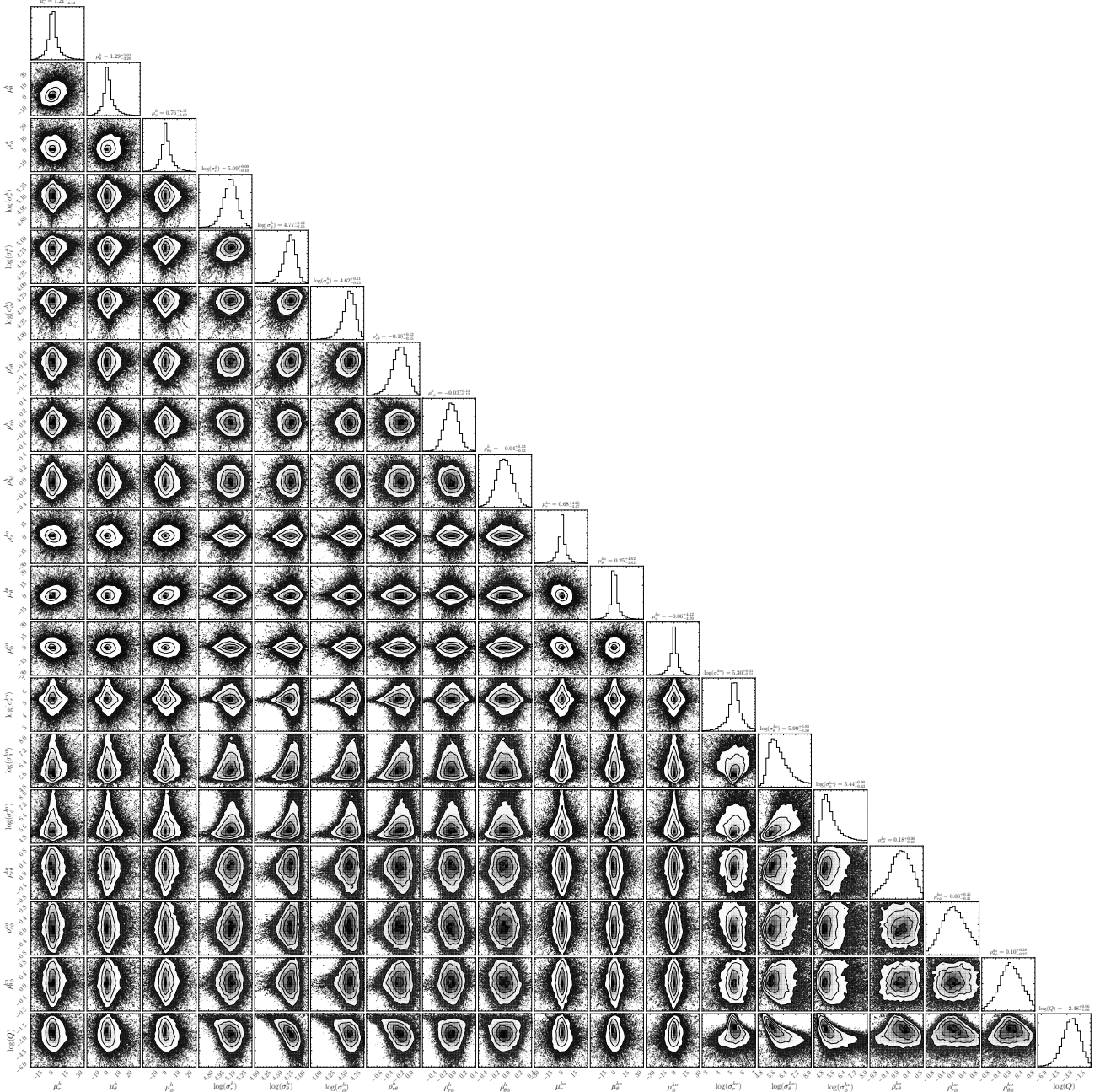


Figure S1. Corner plot for the $[\text{Fe}/\text{H}] < -1.5$ analysis. See Sec. 3 for more details.

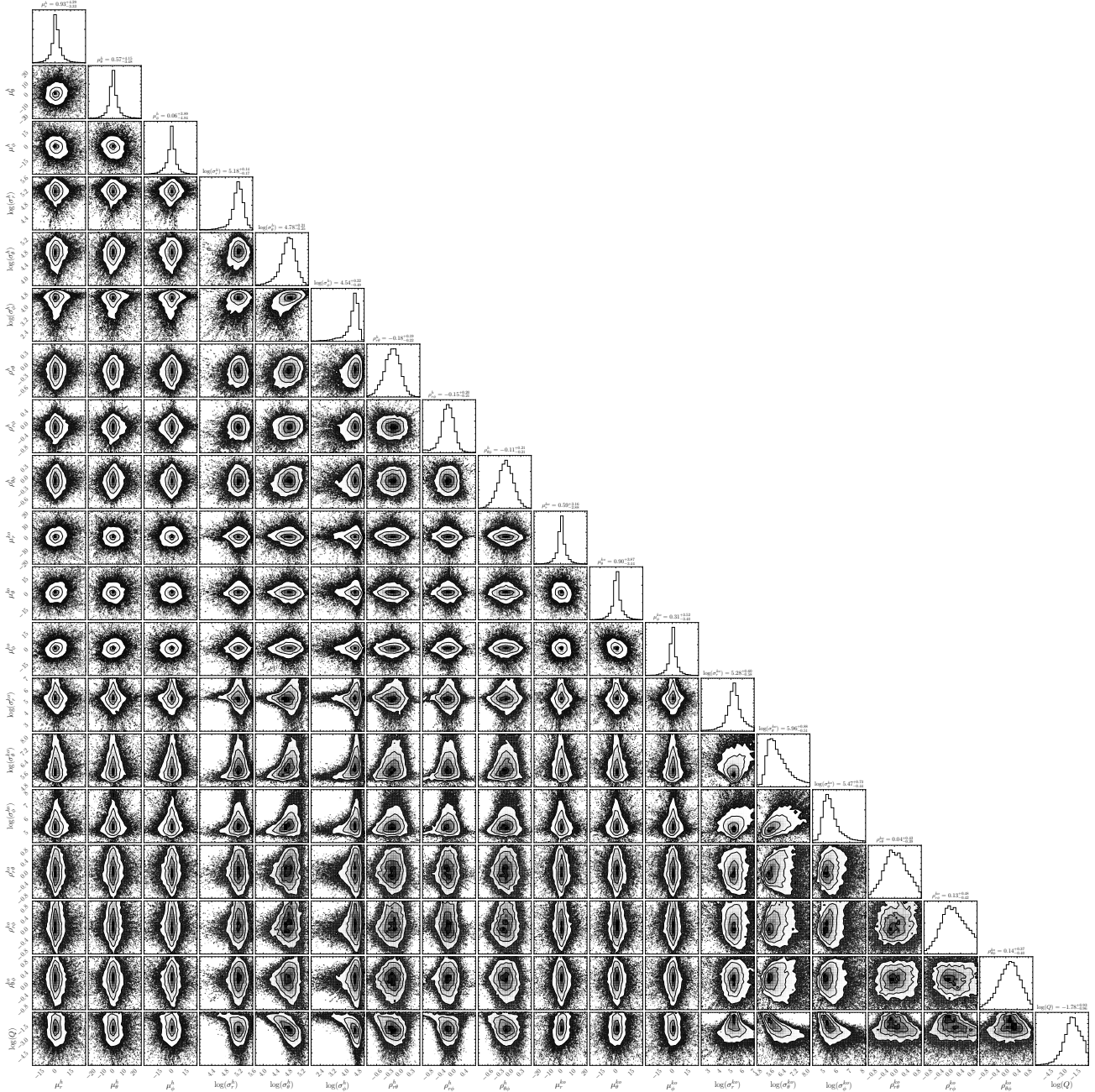


Figure S2. Corner plot for the $[\text{Fe}/\text{H}] < -1.8$ analysis. See Sec. 3 for more details.

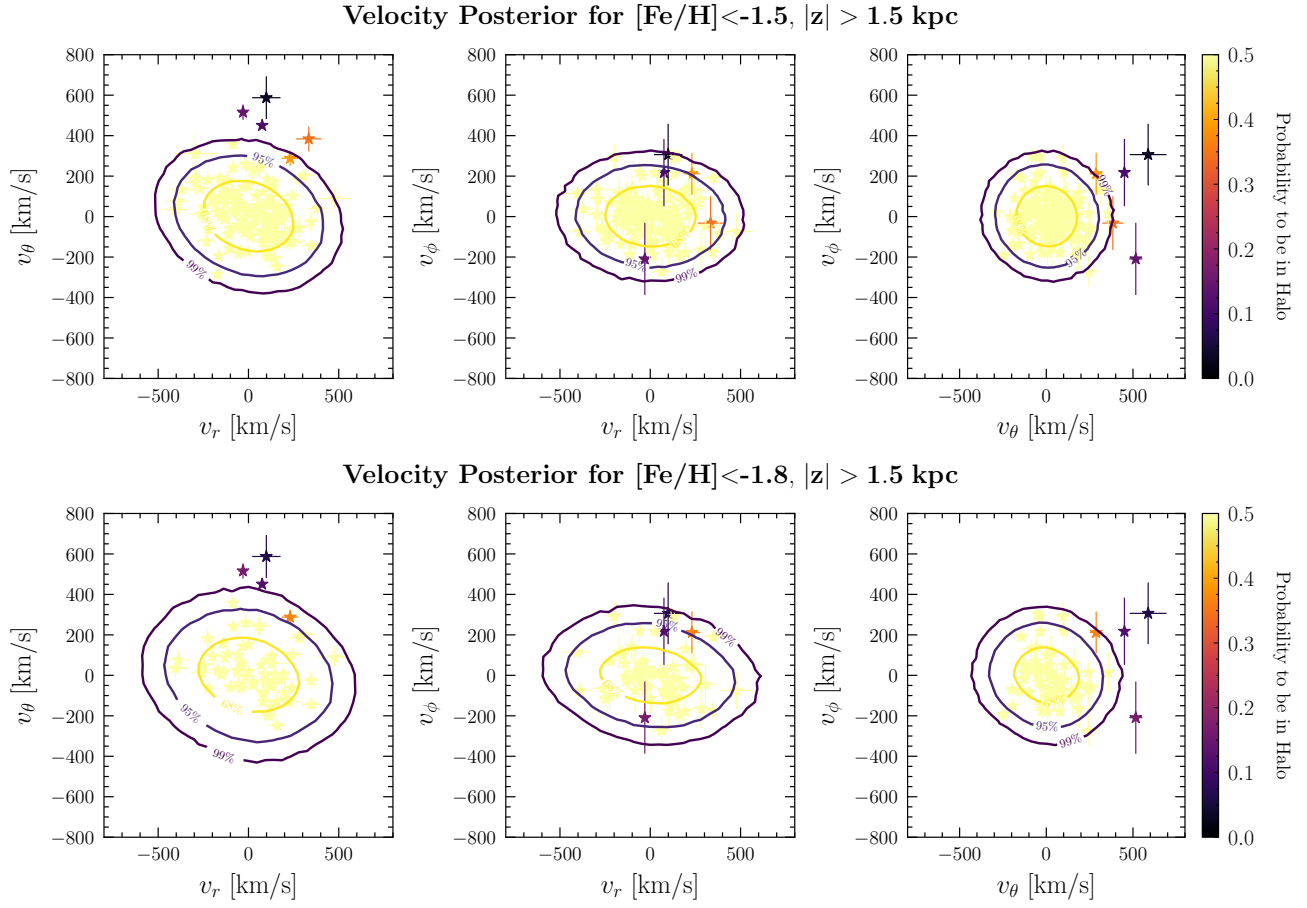


Figure S3. The same as Fig. 2 in the main text, except that we now show all stars that pass the metallicity and $|z| > 1.5$ kpc cuts. Each star’s color indicates its probability of belonging to the halo; note that all stars with probability > 0.5 are indicated in yellow. The stars with the lowest probabilities tend to be located outside the 99% halo contour.

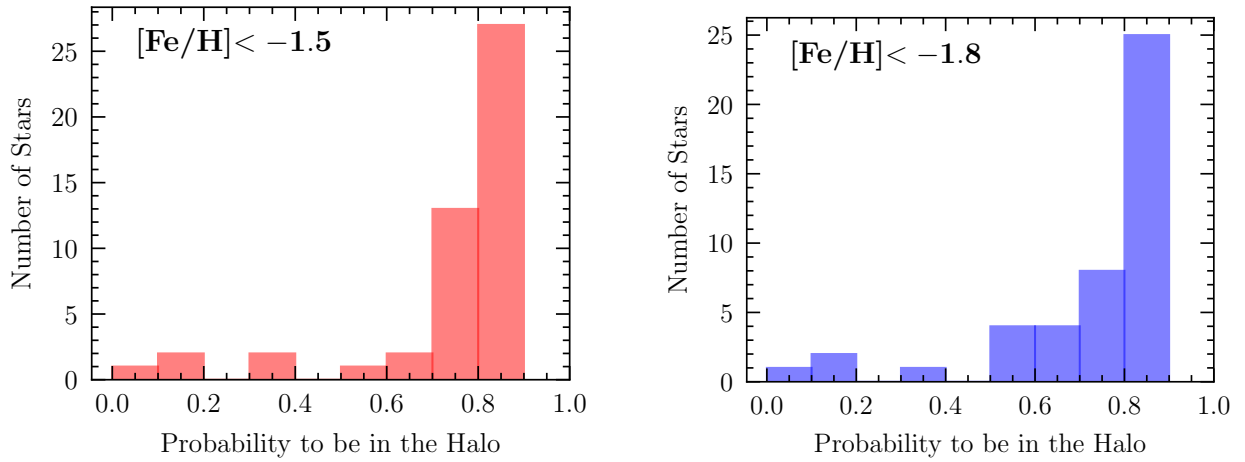


Figure S4. Probability of the stars to belong to the halo, relative to the outlier population, for the $[\text{Fe}/\text{H}] < -1.5$ (left) and $[\text{Fe}/\text{H}] < -1.8$ (right) analyses. We note the presence of two separate populations over and below the 50% cutoff.

TGAS ID	α ($^{\circ}$)	δ ($^{\circ}$)	[Fe/H] (dex)	v_r (km/s)	v_{θ} (km/s)	v_{ϕ} (km/s)	μ_{RA} (mas)	μ_{DE} (mas)	HRV (km/s)	$\log(g)$	T_{eff} (10^3K)	G-band (Mag)	Distance (kpc)
* [†] 20070811_1523m09_120	231.504	-9.19408	-2.56	$75.7^{+15.0}$	451^{+166}	$218^{+16.1}$	$-22.6^{+0.8}$	$-28.0^{+0.4}$	$-165^{+1.19}$	0.09	4.36	10.6	$4.2^{+1.0}$
* [†] 20071017_2109m51_072	316.494	-49.326	-2.13	$231^{+46.0}$	288^{+104}	$212^{+37.2}$	$14.2^{+0.5}$	$-26.9^{+1.1}$	$213^{+1.0}$	0.58	4.49	10.5	$4.1^{+0.8}$
* 20080919_2308m32_143	347.004	-33.6352	-1.69	$334^{+70.0}$	384^{+132}	$-32.2^{+60.7}$	$22.4^{+1.8}$	$-18.7^{+1.2}$	$10.1^{+1.1}$	0.34	4.6	11.4	$5.1^{+1.1}$
* [†] 20090812_2213m50_037	328.962	-51.0937	-1.97	$-30.2^{+25.3}$	516^{+178}	$-209^{+37.5}$	$-0.26^{+0.40}$	$-45.3^{+0.95}$	$-31.8^{+0.55}$	0.95	4.59	11.4	$3.6^{+0.9}$
* [†] 20100124_1148m06_070	176.17	-4.16422	-2.09	$99.0^{+78.5}$	587^{+152}	306^{+106}	$-21.6^{+2.38}$	$-34.6^{+0.9}$	$292^{+1.0}$	0.95	4.73	10.7	$4.4^{+1.0}$

Table S1. List of kinematic outliers found in the analysis of Sec. 4. Stars with the sign * have been found in the analysis with $[\text{Fe}/\text{H}] < -1.5$, while those with the symbol [†] are found in the $[\text{Fe}/\text{H}] < -1.8$ study.